Paradigm Academic Press
Innovation in Science and Technology
ISSN 2788-7030
MAY. 2023 VOL.2, NO.3

Robust Control Method Design for Underactuated Double-Pendulum Overhead Cranes

Tianshi Zhang[1]

[1] University of York

Correspondence: Tianshi Zhang, University of York.

doi:10.56397/IST.2023.05.02

Abstract

Overhead travelling cranes are infrastructure for building construction and their main purpose is to ensure accurate and rapid transport of goods to a given location in the shortest possible time without any residual oscillation. The overhead crane is also a typical underdrive method, which has fewer inputs than the amount being controlled. In some practical applications, uneven weight and f-loads on the hook can lead to load and hook oscillations and the bridge crane can develop the so-called double-pendulum properties. This leads to a high degree of coupling and a high degree of non-linearity between the various state variables of the crane system.

The study that follows suggests a new energy-coupled control strategy for an underactuated double-pendulum overhead crane with initial control force constraints. Strong robustness and superior control performance to parameter changes and external disturbances are the proposed controller's noticeable characteristics. To ensure the smooth start of the trolley, a robust control adds the hyperbolic tangent function to the control procedure.

In addition, the stability analysis and stability verification of the control system is given by using the LaSalle's invariance principle and Lyapunov techniques. The simulation results show that the new energy coupling control method has stability and strong robustness under various conditions such as different rope lengths, load quality, target position and external disturbance when the initial control force decreases.

Keywords: Under-actuated system, robustness, hyperbolic tangent function, Lyapunov techniques, LaSalle's invariance, double-pendulum properties.

1. Introduction

Cranes are frequently utilised in manufacturing tasks as a result of the quick expansion of numerous industries in society. (Neitzel, 2001). As a mechanical device for operations such as the delivery, lifting and loading of goods, cranes are widely used in several scenarios such as factories and construction sites (Ramli, 2017). Among the various types of cranes, the bridge crane is one of the more typical and common ones (Lee, 1998). Overhead cranes, tower cranes, slewing jib cranes, gantry cranes, etc. are mainly used in production and construction (Vaughan, 2010). The main purpose of crane operations is to transport goods precisely to their destination in the shortest possible time (Ngo, 2010).

When a dolly carries a load, the dolly oscillates when coupled to the load and there is a strongly coupled non-linear relationship between the oscillation of the dolly and the load (Guo, 2023). Furthermore, external disturbances, such as mechanical friction and wind, can also have an impact on the accuracy of the transported load in the transport and can even lead to collisions or overturning of the load, which can lead to major safety accidents (Tam, 2011). A lot of work has been done by researchers to eliminate oscillations and accurate positioning, and many important results have been achieved. When the load being transported is too large or the weight is unevenly distributed, the load and hook will swing, creating a "double-pendulum" characteristic. This

phenomenon complicates the dynamic model of the crane, making it highly non-linear, underdriven and coupled with a high degree of coupling between the various states (Li, 2021).

Most research on overhead crane control has focused on the suppression of load swing angles and the precise positioning of the trolley (Al-Garni, 1995). The two main points are the requirement to keep the load swing angle as small as possible when the load is being pulled by the trolley and, in particular, the requirement to suppress residual oscillations when the trolley reaches its designated location. The requirement for the dolly to arrive at the specified position accurately. Based on existing research results, control methods for bridge cranes are generally open-loop control methods such as off-line trajectory planning (Sun, 2011) (Zhang, 2014), optimal control (Sakawa & Shindo, 1982) (Manson, 1982), command shaping (Lewis, 1998) (Hong, 2003) and PID-type control methods (Solihin, 2010) (Solihin, 2008), sliding mode control (Wu, 2020) (Wang, 2021) (Zhang, 2019), adaptive control (Fang, 2011) (He, 2013) (Butler, 1991), robust control (Golovin, 2019) (Sano, 2011), intelligent control (Li, 2012) (Yavuz, 2021) (Smoczek & Szpytko, 2008) (Wang, 2017) and other closed-loop control methods.

This paper derives the dynamics equations for an overhead crane using a known model of a two-pendulum overhead crane (Singhose, 1998). The double-pendulum bridge crane is also investigated using a robust control method. The adopted robust control system ensures a smooth start of the dolly and solves the problem that the amplitude of the load pendulum angle increases with longer transport distance in other control methods. Unlike existing robust control methods, the controller was introduced with a hyperbolic tangent function to reduce the initial control force (Xiao, 2005). The three control parameters designed in the adopted robust control method were then adjusted to achieve better control. The stability analysis and stability verification of the control system are given using Liapunov's method (Chen, 2006) and Russell's invariance principle (Zhang, 2019), respectively (Miao, 2022). Finally, simulations were carried out using the Simulink module in Matlab to build the corresponding models and validate the models (Karris, 2006). After the model was built, the parameters of the control system were adjusted and compared with the PD control method to achieve the best control effect (Vaughan, 2011). It was found that the new robust controller proposed in this paper is stable and robust under various conditions such as different lanyard lengths, load masses, target locations and external disturbances.

(1) The structure of newly designed robust controller is simpler and it can be easily implemented to use in crane systems;

(2) By applying the hyperbolic tangent function to the controller, the initial control force is reduced;

(3) Greater resistance to interference.

2. Problem Statement

This study addresses the control of a double-pendulum overhead crane with fixed sling length.

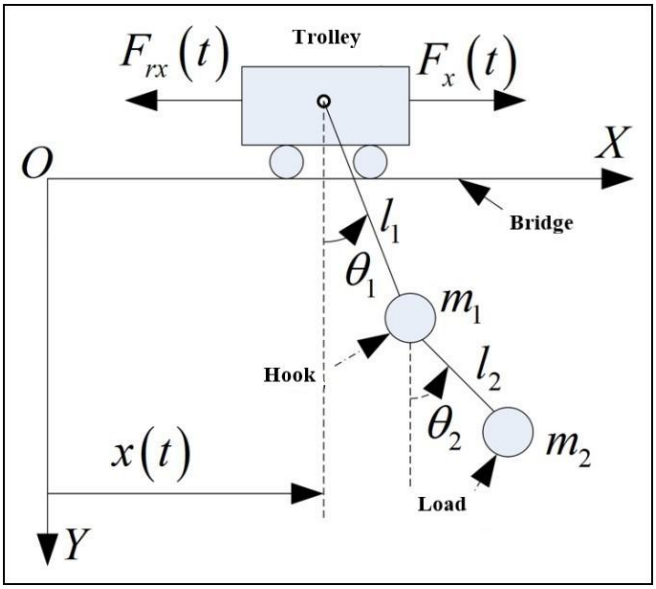

Figure 1. Model crane drawing

A double-pendulum overhead crane with a suspended load is shown in Fig 1. It consists of a dolly moved along the X direction (horizontal direction) by the application of a controlled force F_x. The length of the halyard from

the dolly to the hook is indicated by l_1, θ_1 indicates the angle of swing of the hook relative to the vertical direction. The load is connected to the hook by a lanyard of length l_2, θ_2 indicates the swing of the load concerning the Y-direction.

Neglecting air resistance, the dynamics of the model can be modelled as:

$$\boldsymbol{M}(\boldsymbol{q})\ddot{\boldsymbol{q}} + \boldsymbol{C}(\boldsymbol{q},\dot{\boldsymbol{q}})\dot{\boldsymbol{q}} + \boldsymbol{G}(\boldsymbol{q}) = \boldsymbol{U} \tag{1}$$

Where $\boldsymbol{q} = [\, x\ \theta_1\ \theta_2]^T \in \boldsymbol{R}^3$ is the system state vector, $\boldsymbol{M}(\boldsymbol{q}) \in \boldsymbol{R}^{3*3}$ denotes the inertia matrix, $\boldsymbol{C}(\boldsymbol{q},\dot{q}) \in \mathrm{R}^{3*3}$ denotes the Coriolis matrix, $\boldsymbol{G}(\boldsymbol{q}) \in \mathrm{R}^3$ is the gravity vector and $\boldsymbol{U} \in \mathrm{R}^{3*3}$ denotes the control input vector, as defined below:

$$\boldsymbol{M}(\boldsymbol{q}) = \begin{bmatrix} M+m_1+m_2 & (m_1+m_2)l_1\cos\theta_1 & m_2 l_2\cos\theta_2 \\ (m_1+m_2)l_1\cos\theta_1 & (m_1+m_2)\,l_1^2 & m_2 l_1 l_2\cos(\theta_1-\theta_2) \\ m_2 l_2\cos\theta_2 & m_2 l_1 l_2\cos(\theta_1-\theta_2) & m_2 l_2^2 \end{bmatrix}$$

$$\boldsymbol{C}(\boldsymbol{q},\dot{\boldsymbol{q}}) = \begin{bmatrix} 0 & -(m_1+m_2)l_1\dot{\theta}_1\sin\theta_1 & -m_2 l_2\dot{\theta}_2\sin\theta_2 \\ 0 & 0 & m_2 l_1 l_2\dot{\theta}_2\sin(\theta_1-\theta_2) \\ 0 & -m_2 l_1 l_2\sin(\theta_1-\theta_2) & 0 \end{bmatrix}$$

$$\boldsymbol{G}(\boldsymbol{q}) = [0 \quad (m_1+m_2)gl_1\sin\theta_1 \quad m_2 g l_2\sin\theta_2]^T$$

$$\boldsymbol{U} = [F_x - F_{rx} \quad 0 \quad 0]^T$$

$$\boldsymbol{q} = [x \quad \theta_1 \quad \theta_2]^T$$

Where Dolly Mass, hook mass and load mass is denoted respectively by M, $m_1, m_2 \in \mathrm{R}^+$; $x \in \mathrm{R}^1$ is the dolly displacement; $F_{rx} \in \boldsymbol{R}^1$ is the non-linear bridge friction. Non-linear bridge friction is described by the following model:

$$F_{rx} = f_{rox}\tanh\left(\frac{\dot{x}}{\varepsilon_x}\right) - k_{rx}|\dot{x}|\dot{x} \tag{2}$$

In equation (2), f_{rox}, ε_x is the static friction correlation coefficient, $k_{rx} \in \boldsymbol{R}^1$ is a parameter associated with viscous friction that can be found by offline experimental testing and data fitting.

Define the combined force exerted on the tram as F.

$$F = F_x - F_{rx} \tag{3}$$

The existence of a skew-symmetric relationship between the inertia matrix M(q) and the Coriolis force matrix C(q,q) can be easily demonstrated.

$$\boldsymbol{v}^T\left(\frac{1}{2}\dot{\boldsymbol{M}}(\boldsymbol{q}) - \boldsymbol{C}(\boldsymbol{q},\dot{\boldsymbol{q}})\right)\boldsymbol{v} = 0, \quad \forall \boldsymbol{v} \in \boldsymbol{R}^3 \tag{4}$$

Figure 1 shows that the load's horizontal displacement has the following expression:

$$x_p = x + l_1\sin\theta_1 + l_2\sin\theta_2 \tag{5}$$

This shows that $x_p(t)$ is the natural coupling signal between $x(t)$,$\theta_1(t)$,$\theta_2(t)$. Inspired by the form of equation (5), the generalised load horizontal displacement signals are introduced to capture $x(t), \theta_1(t), \theta_2(t)$ as follows:

$$X_p = x + \lambda_1\sin\theta_1 + \lambda_2\sin\theta_2 \tag{6}$$

Where λ_1 and λ_2 are the parameters to be adjusted.

The following presumptions are made to maintain generality:

Assumption 1. The mass of the sling is not taken into account and it is also assumed that the sling always remains unbent at all times. Furthermore, the length of the sling is always constant during transport.

Assumption 2. The load is always under the dolly during the transport of the goods.

Demonstrate the following:

$$-\frac{\pi}{2} < \theta_1, \quad \theta_2 < \frac{\pi}{2}, \quad \forall t \geq 0 \tag{7}$$

3. Controller Development and Stability Analysis

3.1 Robust Controller Design

After studying the passive characteristics of the crane and the generalised payload horizontal displacement signal, a new energy-coupled controller based on initial control is proposed. In this study, a detailed mathematical analysis

is used to develop a new class of energy functions. Additionally, by lowering the system's initial control force, a hyperbolic tangent function is added to the control strategy to guarantee a smooth start of the dolly.

The equation below expressed the system energy that includes both kinetic and potential energy:

$$E(t) = \frac{1}{2}\dot{q}^{T}M(q)\dot{q} + (m_1 + m_2)gl_1(1-\cos\theta_1) + m_2gl_2(1-\cos\theta_2) \tag{8}$$

The resulting equation, by taking the derivative equation (8) concerning time and then substituting it with equation (3) is as follows;

$$\begin{aligned}\dot{E}(t) &= \dot{\boldsymbol{q}}^{T}\left(\boldsymbol{M}(\boldsymbol{q})\ddot{\boldsymbol{q}} + \frac{1}{2}\boldsymbol{M}(\boldsymbol{q})\dot{\boldsymbol{q}}\right) + (m_1+m_2)gl_1\dot{\theta}_1\sin\theta_1 + m_2gl_2\dot{\theta}_2\sin\theta_2 \\ &= \dot{\boldsymbol{q}}^{T}\left(\boldsymbol{U} - \boldsymbol{G}(\boldsymbol{q}) - \boldsymbol{C}(\boldsymbol{q},\dot{\boldsymbol{q}})\dot{\boldsymbol{q}} + \frac{1}{2}\boldsymbol{M}(\boldsymbol{q})\dot{\boldsymbol{q}}\right) + (m_1+m_2)gl_1\dot{\theta}_1\sin\theta_1 + m_2gl_2\dot{\theta}_2\sin\theta_2 \\ &= \dot{\boldsymbol{x}}^{T}\left(F_x - F_{rx}\right) \\ &= \dot{\boldsymbol{x}}^{T}F\end{aligned} \tag{9}$$

This proves the passive energy cancellation for F(t) and x(t) systems. Equation (9) shows that there are no relevant terms for θ_1 (or $\dot{\theta}_1$) and θ_2 (or $\dot{\theta}_2$) in $\dot{E}(t)$. An energy-like storage function => E t(t) is created to improve the system's transient control performance and to address this phenomenon. Its time derivative may be described using the system dynamics model as follows:

$$\dot{E}_t(t) = \dot{X}_p F = \dot{E} + \dot{E}_{k_1} + \dot{E}_{k2} \tag{10}$$

Here X_p is defined as equation (10). Taking the time derivative of equation (10) gives the following result:

$$\dot{X}_p = \dot{x} + \lambda_1\dot{\theta}_1\cos\theta_1 + \lambda_2\dot{\theta}_2\cos\theta_2 \tag{11}$$

Equations (1) and (11) can be simply substituted into equation (10), and it results that:

$$\begin{aligned}\dot{E}_{K_1} &= \lambda_1\dot{\theta}_1\cos\theta_1 F \\ &= -(M+m_1+m_2)\lambda_1 l_1\dot{\theta}_1\ddot{\theta}_1 + \lambda_1\dot{\theta}_1\cos\theta_1(m_1+m_2)l_1\left(\cos\theta_1\ddot{\theta}_1 - \dot{\theta}_1^{2}\sin\theta_1\right) \\ &\quad -(M+m_1+m_2)\lambda_1 g\sin\theta_1\dot{\theta}_1 - \frac{M+m_1+m_2}{m_1+m_2}m_2\lambda_1 l_2\sin\theta_1\sin\theta_2\dot{\theta}_1\ddot{\theta}_2 \\ &\quad -\frac{M}{m_1+m_2}m_2\lambda_1 l_2\cos\theta_1\cos\theta_2\dot{\theta}_1\ddot{\theta}_2 + \frac{M}{m_1+m_2}m_2\lambda_1 l_2\cos\theta_1\sin\theta_2\dot{\theta}_2^{2}\dot{\theta}_1 \\ &\quad -\frac{M+m_1+m_2}{m_1+m_2}m_2\lambda_1 l_2\sin\theta_1\cos\theta_2\dot{\theta}_1\dot{\theta}_2^{2}\end{aligned} \tag{12}$$

$$\begin{aligned}\dot{E}_{K_2} &= \lambda_2\dot{\theta}_2\cos\theta_2 F \\ &= -(M+m_1+m_2)\lambda_2 l_2\dot{\theta}_2\ddot{\theta}_2 + m_2\lambda_2\dot{\theta}_1\cos\theta_2 l_2\left(\cos\theta_2\ddot{\theta}_2 - \dot{\theta}_2^{2}\sin\theta_2\right) \\ &\quad -(M+m_1+m_2)\lambda_2 g\sin\theta_2\dot{\theta}_2 - M\lambda_2 l_1\cos\theta_1\cos\theta_2\dot{\theta}_2\ddot{\theta}_1 \\ &\quad -(M+m_1+m_2)\lambda_2 l_1\sin\theta_1\sin\theta_2\dot{\theta}_2\ddot{\theta}_1 + M\lambda_2 l_1\sin\theta_1\cos\theta_2\dot{\theta}_1^{2}\dot{\theta}_2 \\ &\quad -(M+m_1+m_2)\lambda_2 l_1\cos\theta_1\sin\theta_2\dot{\theta}_2\dot{\theta}_1^{2}\end{aligned} \tag{13}$$

Therefore, based on equations (12) & (13) structure, the relationship between λ_1 and λ_2 is assumed to be:

$$\frac{M}{m_1+m_2}m_2\lambda_1 l_2 = M\lambda_2 l_1 \Rightarrow \frac{\lambda_1}{\lambda_2} = \frac{(m_1+m_2)l_1}{m_2 l_2} \tag{14}$$

Based on equation (14), equation (12)(13) can be rewritten as:

$$\begin{aligned}\dot{E}_{K_1}+\dot{E}_{K_2}=&-\left(M+m_1+m_2\right)\lambda_1 l_1\dot{\theta}_1\ddot{\theta}_1+\lambda_1\dot{\theta}_1\cos\theta_1\left(m_1+m_2\right)l_1\left(\cos\theta_1\ddot{\theta}_1-\dot{\theta}_1^{\,2}\sin\theta_1\right)\\&-\left(M+m_1+m_2\right)\lambda_1 g\sin\theta_1\dot{\theta}_1-m_2\lambda_2 l_2\cos\theta_2\dot{\theta}_2\left(\ddot{\theta}_2\cos\theta_2-\dot{\theta}_2^{\,2}\sin\theta_2\right)\\&-\left(M+m_1+m_2\right)\lambda_2 g\sin\theta_2\dot{\theta}_2-\left(M+m_1+m_2\right)\lambda_2 l_2\dot{\theta}_2\ddot{\theta}_2\\&-M\lambda_2 l_1\frac{d}{dt}\left(\dot{\theta}_1\dot{\theta}_2\cos\theta_1\cos\theta_2\right)-\left(M+m_1+m_2\right)l_1\lambda_2\frac{d}{dt}\left(\dot{\theta}_1\dot{\theta}_2\sin\theta_1\sin\theta_2\right)\end{aligned}\tag{15}$$

The time integration of equation (15) gives:

$$\begin{aligned}E_{K_1}+E_{K_2}=&-\frac{1}{2}\left(M+m_1+m_2\right)\left(\lambda_1 l_1\dot{\theta}_1^2+\lambda_2 l_2\dot{\theta}_2^2\right)+\frac{1}{2}\left(m_1+m_2\right)\lambda_1 l_1\dot{\theta}_1^2\cos^2\theta_1\\&+\frac{1}{2}m_2\lambda_2 l_2\dot{\theta}_1^2\theta_2\cos^2\theta_2-M\lambda_2 l_1\left(\dot{\theta}_1\dot{\theta}_2\cos\theta_1\cos\theta_2\right)\\&-\left(M+m_1+m_2\right)l_1\lambda_2\left(\dot{\theta}_1\dot{\theta}_2\sin\theta_1\sin\theta_2\right)\\&-\left(M+m_1+m_2\right)g\left[\lambda_1\left(1-\cos\theta_1\right)+\lambda_2\left(1-\cos\theta_2\right)\right]\end{aligned}\tag{16}$$

It follows easily from equation (14) that when λ_1, $\lambda_2<0$:

$$\lambda_1 l_1\lambda_2 l_2=\frac{(m_1+m_2)}{m_2}l_1^2\lambda_2^2>l_1^2\lambda_2^2\tag{17}$$

According to equation (17) and the algebraic-geometric mean inequality, from equation (16), we get:

$$\begin{aligned}E_{K_1}+E_{K_2}=&-\frac{1}{2}(M+m_1+m_2)\left(\lambda_1 l_1\dot{\theta}_1^{\,2}+\lambda_2 l_2\dot{\theta}_2^{\,2}\right)\\&-(M+m_1+m_2)l_1\lambda_2\left(\dot{\theta}_1\dot{\theta}_2\,sin\,\theta_1\,sin\,\theta_2\right)\\&-\frac{1}{2}M\left(\lambda_1 l_1\dot{\theta}_1^{\,2}\,cos^2\,\theta_1+\lambda_2 l_2\dot{\theta}_2^{\,2}\,cos^2\,\theta_2\right)\\&-Ml_1\lambda_2\left(\dot{\theta}_1\dot{\theta}_2\,cos\,\theta_1\,cos\,\theta_2\right)-\frac{1}{2}m_1\lambda_2 l_2\dot{\theta}_2^{\,2}\,cos^2\,\theta_2\\&-(M+m_1+m_2)g[\lambda_1(1-cos\,\theta_1)+\lambda_2(1-cos\,\theta_2)]\geq 0\end{aligned}\tag{18}$$

Equation (11) shows that:

$$E_t(t)=E+E_{k_1}+E_{k_2}\geq 0\tag{19}$$

The following generalised payload positioning error ξ_x is introduced for facilitating subsequent controller development and analysis;

$$\xi_x=X_p-p_d=x-p_d+\lambda_1\,sin\,\theta_1+\lambda_2\,sin\,\theta_2=e_x+\lambda_1\,sin\,\theta_1+\lambda_2\,sin\,\theta_2\tag{20}$$

In the equation, $p_d\in\boldsymbol{R}^+$represents the desired target position and $e_x\in\boldsymbol{R}^1$represents the dolly positioning error. And e_x is:

$$e_x=x-p_d\tag{21}$$

Differentiating the time of equation (20) gives the following results.

$$\dot{\xi}_x=\dot{X}_p=\dot{e}_x+\lambda_1\dot{\theta}_1\,cos\,\theta_1+\lambda_2\dot{\theta}_2\,cos\,\theta_2\tag{22}$$

From equations (10) and (11) we have:

$$\dot{E}_t(t)=\dot{\xi}_x F\tag{23}$$

Given equation (23) structure, the energy-based coupled controller with initial control force constraints is designed, which is as follows:

$$F_x=F_{rx}-k_p\,tanh(\xi_x)-k_d\dot{\xi}_x\tag{24}$$

Hyperbolic tangent functions are a class of functions with double-curve properties. Hyperbolic functions are similar to trigonometric functions and can be divided into six categories: hyperbolic sine, hyperbolic cotangent, hyperbolic cotangent, hyperbolic tangent, hyperbolic tangent, hyperbolic tangent and hyperbolic cotangent. In mathematical language, hyperbolic tangent functions are often referred to as $tanh$, or simplified as th. The hyperbolic tangent function is calculated similarly to the tangent function by dividing the hyperbolic sine by the hyperbolic cosine, or $tanh(x) = \frac{sinh(x)}{cosh(x)}$. When x is large in absolute value, its curve approaches between $y = 1$ and $y = -1$, in the 1st quadrant the curve $y = 1$ and in the 3rd quadrant $y = -1$. That is, the hyperbolic tangent function has values in the range (-1,1).

With zero initial condition x the following occurs.

$$x(0) = 0, \quad \dot{x}(0) = 0, \quad \theta_1(0) = \theta_2(0) = 0, \quad \dot{\theta}_1(0) = \dot{\theta}_2(0) = 0 \rightarrow F_{rx} = 0, \quad \dot{\xi}_x = 0, \quad \xi_x = -p_d \tag{25}$$

Calculating the initial control force from equation (24) gives:

$$|F_x(t)| = \left|k_p \, tanh(-p_d)\right| \leq k_p \, min\{\,|p_d|\,,\ 1\} \tag{26}$$

Hence, the following is proven if the dolly's desired position is far from its starting point:

$$|e_x(0)| = p_d \gg 1 \tag{27}$$

The proposed controller (24) can effectively reduce the initial control volume of the crane system, achieve a smooth start of the dolly, reduce the acceleration generated by the force on the dolly and solve the problem that the amplitude of the load swing angle increases as the transport distance becomes longer.

3.2 Stability Analysis

The constructed controller (24) makes sure that the system state steadily approaches and converges to the equilibrium point, as shown by the description of the following theorem.

Theorem 1: The desired position p_d can be precisely driven by the dolly. The controller allows for rapid suppression and elimination of $\theta_1(t)$ and $\theta_2(t)$ (24).

$$\lim_{t\to\infty}\left[x(t) \quad \dot{x}(t) \quad \theta_1(t) \quad \dot{\theta}_1(t) \quad \theta_2(t) \quad \dot{\theta}_2(t)\right]^T = [p_d \quad 0 \quad 0 \quad 0 \quad 0 \quad 0]^T \tag{28}$$

Note: In practice, $\theta_1(t)$ and $\theta_2(t)$ are usually kept within 10° due to the limitations of the dolly acceleration, in which case the approximate results are as follows:

$$sin\,\theta_1 \approx \theta_1, \quad sin\,\theta_2 \approx \theta_2, \quad cos\,\theta_1 \approx 1, \quad cos\,\theta_2 \approx 1 \tag{29}$$

Proof: The following Liapunov function has been used to demonstrate the aforementioned theorem:

$$V(t) = E_t(t) + k_p \, ln[cosh(\xi_x)] \tag{30}$$

Calculate equation (30) based on the time derivatives of the trajectories of equations (23) and (24).

$$\dot{V}(t) = -k_d \dot{\xi}_x^2 \leq 0 \tag{31}$$

V(t) is decreasing because V(t) is negative definite, indicating that the proposed closed-loop system is Liapunov stable at the origin. V(t) is therefore bound, in other terms.

$$V(t) \in L_\infty \tag{32}$$

Thus, it can be derived from equations (2), (11), (20), (22), (24), (30) and (32).

$$\dot{x},\ \dot{\theta}_1,\ \dot{\theta}_2,\ F_x,\ F_{rx},\ \xi_x,\ \dot{\xi}_x,\ e_x,\ \dot{e_x} \in L_\infty \tag{33}$$

To prove this conclusion completely, we define:

$$\varphi = \{x, \quad \dot{x}, \quad \theta_1, \quad \dot{\theta}_1, \quad \theta_2, \quad \dot{\theta}_2 | \dot{V}(t) = 0\} \tag{34}$$

Define *S*as the largest invariant set contained in φ.

Thus, in S:

$$\dot{\xi}_x = \dot{x} + \lambda_1 \dot{\theta}_1 \, cos\,\theta_1 + \lambda_2 \dot{\theta}_2 \, cos\,\theta_2 = 0 \tag{35}$$

From (35) it can be readily concluded that:

$$\xi_x = e_x + \lambda_1 \, sin\,\theta_1 + \lambda_2 \, sin\,\theta_2 = \alpha \tag{36}$$

$$\text{And } \ddot{\xi}_x = \ddot{x} + \lambda_1 \ddot{\theta}_1 \, cos\,\theta_1 - \lambda_1 \dot{\theta}_1^2 \, sin\,\theta_1 + \lambda_2 \ddot{\theta}_2 \, cos\,\theta_2 - \lambda_2 \dot{\theta}_2^2 \, sin\,\theta_2 = 0 \tag{37}$$

The following equations hold when equations (35) and (36) are substituted into equation (24):

$$F_x - F_{rx} = -k_p tanh\alpha \tag{38}$$

From equation (37) it follows that:

$$\lambda_1\ddot{\theta}_1 \cos\theta_1 - \lambda_1\dot{\theta}_1^2 \sin\theta_1 + \lambda_2\ddot{\theta}_2 \cos\theta_2 - \lambda_2\dot{\theta}_2^2 \sin\theta_2 = -\ddot{x} \tag{39}$$

After rearrangement, equation (1) can become:

$$\begin{aligned} &\cos\theta_1\ddot{\theta}_1 - \dot{\theta}_1^{\,2}\sin\theta_1 + \frac{m_2 l_2}{(m_1+m_2)l_1}\left(\ddot{\theta}_2\cos\theta_2 - \dot{\theta}_2^{\,2}\sin\theta_2\right) \\ &= \frac{1}{(m_1+m_2)l_1}\left[F - (M+m_1+m_2)\dot{x}\right] \end{aligned} \tag{40}$$

This is consistent with the findings of equations (14) and (40), which suggest that:

$$\ddot{x} = -\frac{k_p\lambda_1}{(m_1+m_2)l_1+(M+m_1+m_2)\lambda_1} tan\, h\alpha \tag{41}$$

Assuming that $\alpha \neq 0$, it is concluded that:

$$\dot{x}(t) \to \begin{cases} +\infty & \alpha<0 \\ -\infty & \alpha<0 \end{cases} \quad \text{when } t \to \infty \tag{42}$$

However, this contradicts the conclusion $\dot{x}(t) \in L_\infty$ in equation (33), so the assumption $\alpha \neq 0$ does not hold. So in S:

$$\alpha = 0 \tag{43}$$

Substituting equation (43) into equations (38) and (41) gives:

$$F_x - F_{rx} = 0,\ \ddot{x} = 0 \to \dot{x} = \dot{e}_x = \beta \tag{44}$$

In the same way, we get:

$$\beta = 0 \to \dot{x} = \dot{e}_x = 0 \tag{45}$$

After substituting equations (29) and (44) into equation (1), equation (1) can be rewritten in the following way:

$$(m_1+m_2)l_1\ddot{\theta}_1 + m_2 l_2\ddot{\theta}_2 = 0 \tag{46}$$

$$(m_1+m_2)l_1\ddot{\theta}_1 + m_2 l_2\ddot{\theta}_2 + (m_1+m_2)g\theta_1 = 0 \tag{47}$$

$$l_1\ddot{\theta}_1 + l_2\ddot{\theta}_2 + g sin\,\theta_2 = 0 \tag{48}$$

From equations (7), (46) and (47) it follows that in *S*:

$$\theta_1 = 0 \tag{49}$$

The first and second-order derivatives in the above equations can be derived as:

$$\dot{\theta}_1 = 0,\ \ddot{\theta}_1 = 0 \tag{50}$$

From equations (46), (48), (49) and (50) it follows that:

$$\theta_2 = 0 \tag{51}$$

The following equations therefore hold in S:

$$\dot{\theta}_2 = 0,\ \ddot{\theta}_2 = 0 \tag{52}$$

Equations (49) and (51) are substituted into equation (36) to produce:

$$e_x = 0 \to x = p_d \tag{53}$$

Equations (45) and (49)-(52) demonstrate this further by stating that only the equilibrium point $\lim_{t\to\infty}\left[x(t)\ \ \dot{x}(t)\ \ \theta_1(t)\ \ \dot{\theta}_1(t)\ \ \theta_2(t)\ \ \dot{\theta}_2(t)\right]^T = [p_d\ \ 0\ \ 0\ \ 0\ \ 0\ \ 0]^T$ is contained in the maximal invariant set S. By invoking the Russell invariance principle, it can be concluded that the system state converges asymptotically to the equilibrium point.

4. Results of the Experiment and Discussion

4.1 Experimental Setup

Simulations are run to confirm the enhanced performance of the suggested control approach and to assess the viability and efficacy of the robust controller for underdriven systems. MATLAB / Simulink are used to implement the numerical simulations.

To verify the simulation results, waveform plots of *X, F,* $F_{rx}, \theta_1, \theta_2$ are output.

From the kinetic equation (1) it follows that:

$$\begin{aligned} F_x - F_{rx} = {} & (M+m_1+m_2)\ddot{x} + (m_1+m_2)l_1 \cos\theta_1\,\ddot{\theta}_1 + m_2 l_2 \cos\theta_2\,\ddot{\theta}_2 \\ & -(m_1+m_2)l_1\dot{\theta}_1 \sin\theta_1\,\dot{\theta}_1 - m_2 l_2\dot{\theta}_2 \sin\theta_2\,\dot{\theta}_2 \end{aligned} \tag{54}$$

According to (54) we can obtain $\ddot{X}$ as:

$$\ddot{x} = \frac{\begin{pmatrix} F_x - F_{rx} - (m_1+m_2) l_1 \cos\theta_1 \ddot{\theta}_1 - m_2 l_2 \cos\theta_2 \ddot{\theta}_2 \\ +(m_1+m_2) l_1 \dot{\theta}_1 \sin\theta_1 \dot{\theta}_1 + m_2 l_2 \dot{\theta}_2 \sin\theta_2 \dot{\theta}_2 \end{pmatrix}}{(M+m_1+m_2)} \tag{55}$$

The simulation is built according to the resulting equation (55), as shown in Figure 2.

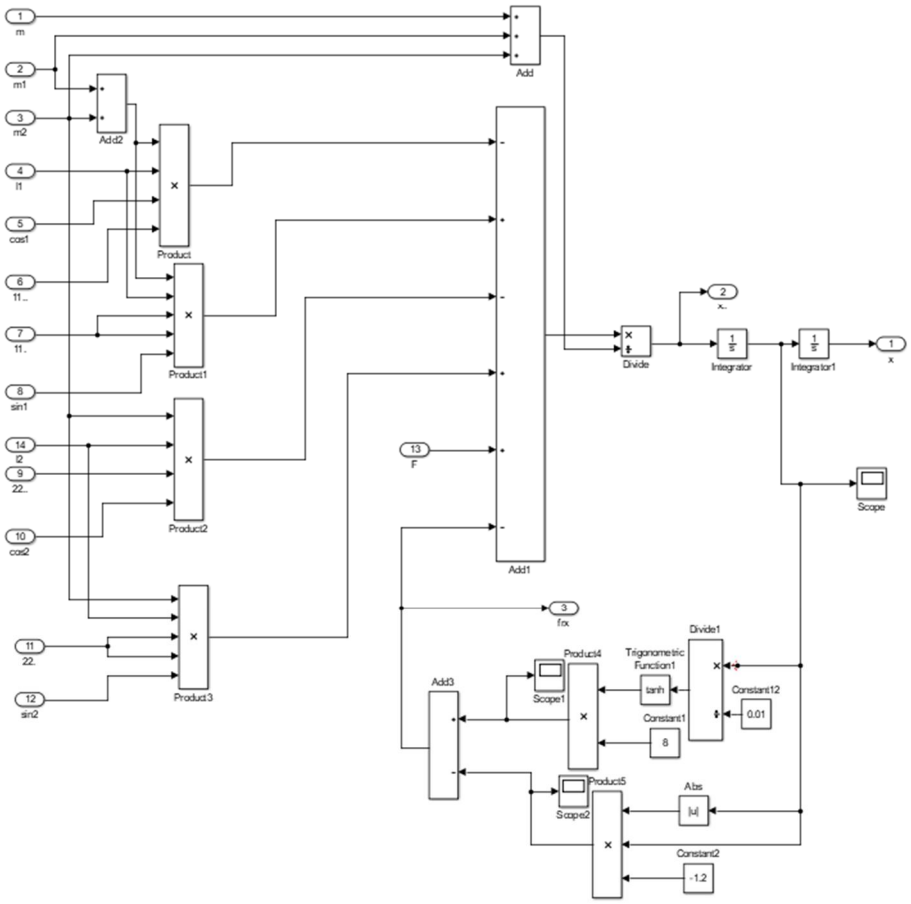

Figure 2. X subroutine simulation module

According to the kinetic equation (1) it is obtained that:

$$\begin{gathered}(m_1+m_2) l_1 \cos\theta_1 \ddot{x} + m_2 l_2 l_1 \ddot{\theta}_2 \cos(\theta_1-\theta_2) + m_2 l_2 l_1 \ddot{\theta}_2 \sin(\theta_1-\theta_2) \dot{\theta}_2 \\ +(m_1+m_2) g l_1 \sin\theta_1 + (m_1+m_2) l_1 \ddot{\theta}_1 l_1 = 0\end{gathered} \tag{56}$$

From (56) it follows that:

$$\ddot{\theta}_1 = \frac{\begin{pmatrix} -(m_1+m_2) l_1 \cos\theta_1 \ddot{x} - m_2 l_2 l_1 \ddot{\theta}_2 \cos(\theta_1-\theta_2) \\ -m_2 l_2 l_1 \ddot{\theta}_2 \sin(\theta_1-\theta_2) \dot{\theta}_2 - (m_1+m_2) g l_1 \sin\theta_1 \end{pmatrix}}{(m_1+m_2) l_1 l_1} \tag{57}$$

The simulation is built according to the resulting equation (57), as shown in Figure 3.

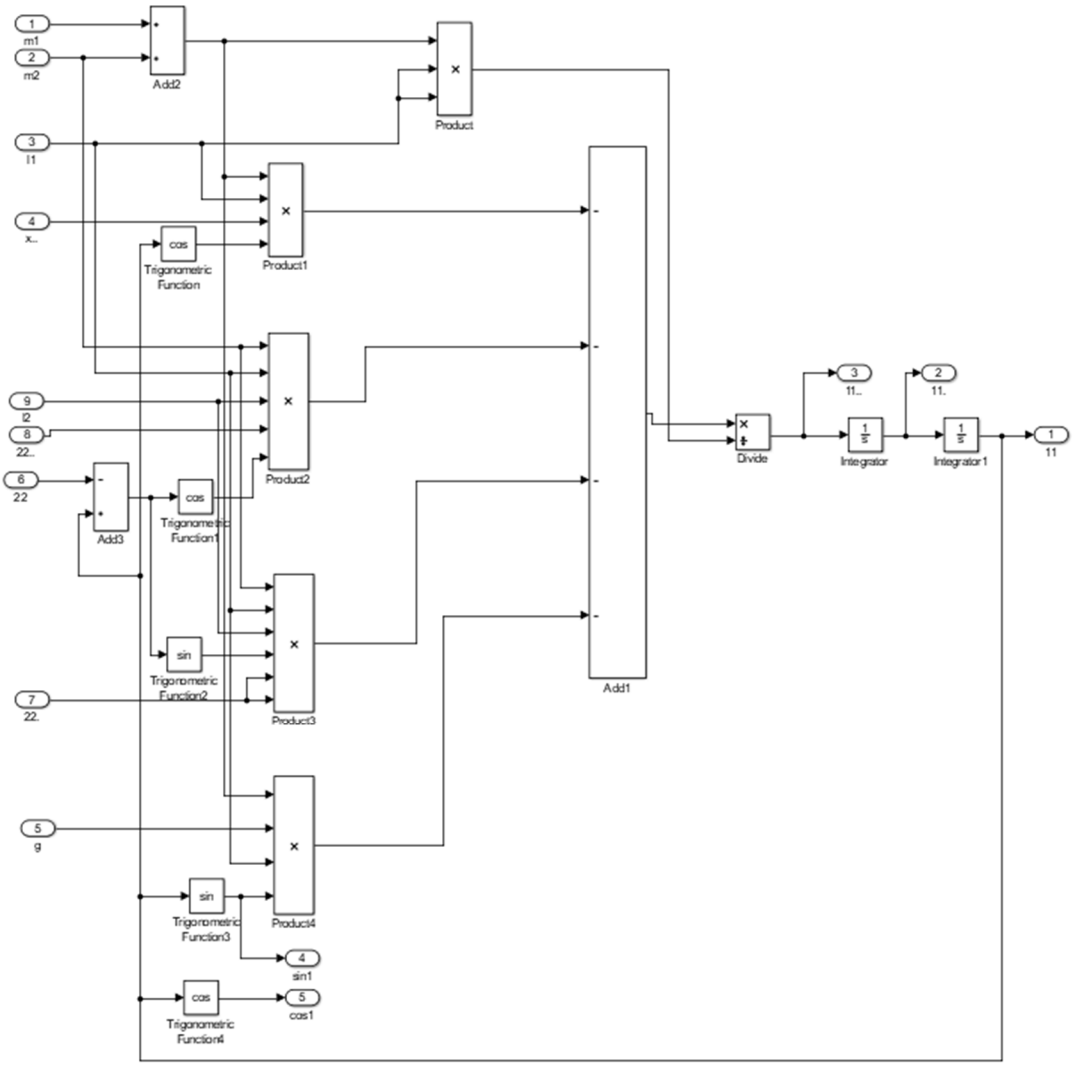

Figure 3. θ_1 program module

Calculated from the kinetic equation (1):

$$m_2 l_2 \ddot{x}\cos\theta_2 + m_2 l_2 l_1 \ddot{\theta}_1 \cos(\theta_1 - \theta_2) - m_2 l_2 l_1 \ddot{\theta}_1 \sin(\theta_1 - \theta_2)\,\ddot{\theta}_1 + m_2 g l_2 \sin\theta_2 + m_2 l_2^2 \ddot{\theta}_2 = 0 \quad (58)$$

From (58) it follows that:

$$\ddot{\theta}_2 = \frac{\left(-m_2 l_2 \ddot{x}\cos\theta_2 - m_2 l_2 l_1 \ddot{\theta}_1 \cos(\theta_1-\theta_2) + m_2 l_2 l_1 \ddot{\theta}_1 \sin(\theta_1-\theta_2)\ddot{\theta}_1\right)}{-m_2 g l_2 \sin\theta_2} \quad (59)$$

The simulation is built according to the resulting equation (59), shown in Figure 4.

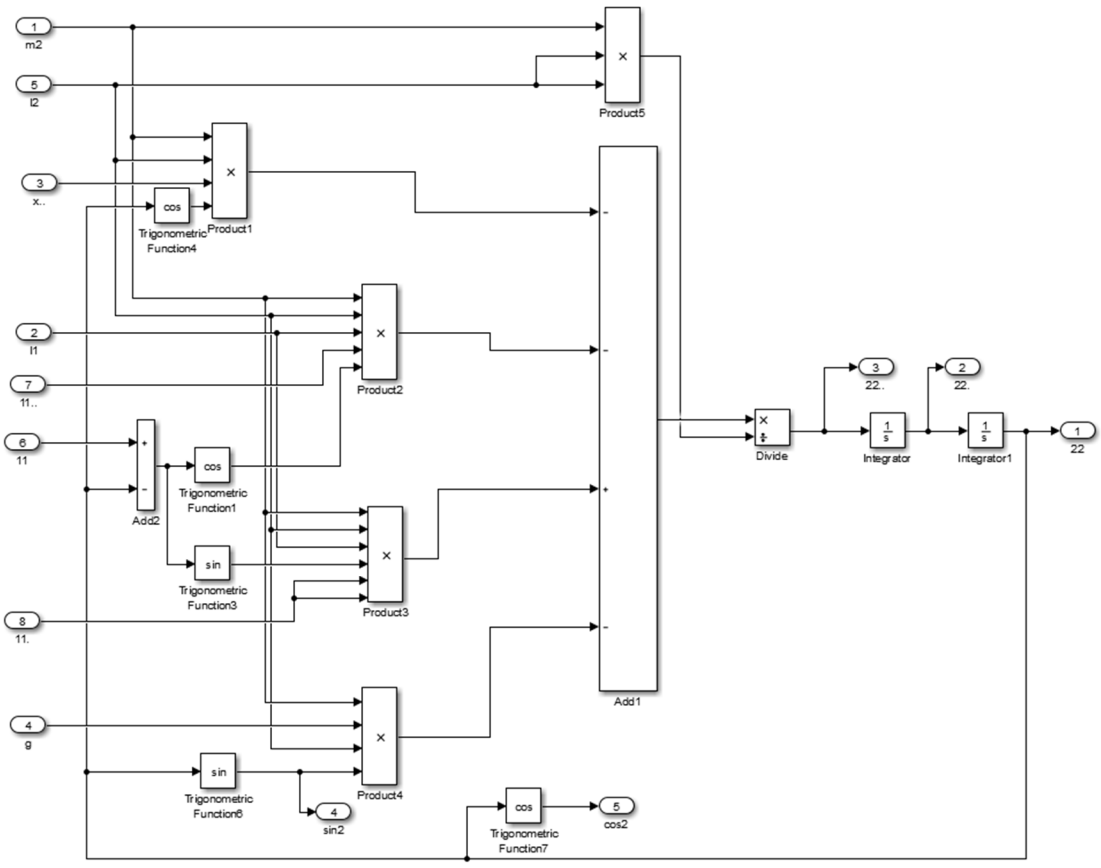

Figure 4. θ_2 subroutine simulation module

The simulation is constructed according to the non-linear bridge friction descriptive equation (2). In this simulation, it is taken that: $k_{rx} = -1.2, \quad f_{rox} = 8, \quad \varepsilon_x = 0.01$.

The simulation is built according to equation (2), as shown in Figure 5.

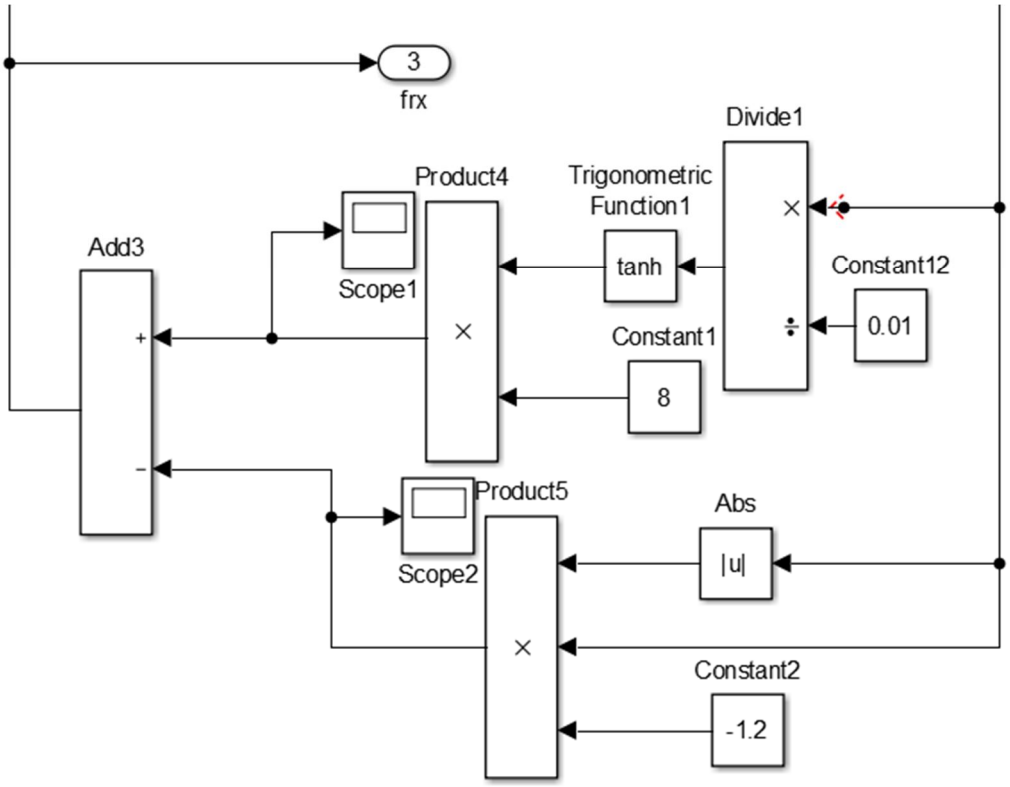

Figure 5. F_{rx} subroutine simulation module

The controller simulation is built according to controller equation (24), as shown in Figure 6.

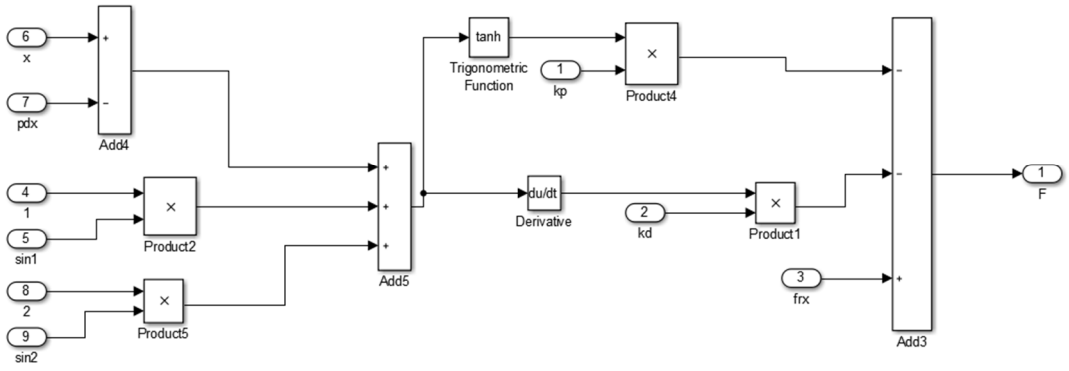

Figure 6. F subroutine simulation module

The total simulation procedure is Figure 7.

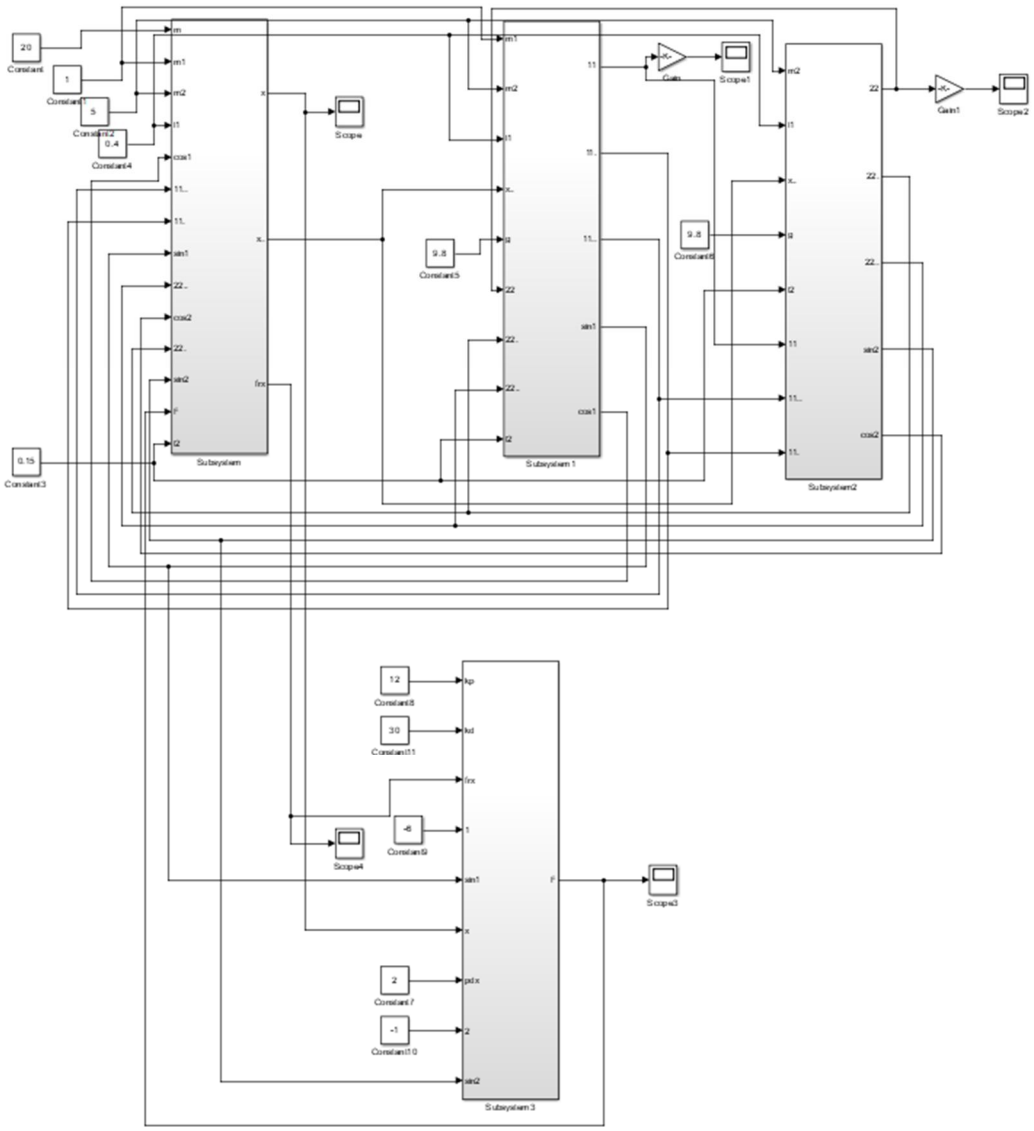

Figure 7. Total simulation procedure

4.2 Comparative Tests

The physical characteristics of the designed system are listed below:

$$M=20\text{kg},\ m_1=1\text{kg},\ m_2=5\text{kg},\ l_1=2\text{m},\ l_2=0.4\text{m},\ g=9.8\text{m/s}^2$$

$X(0), \theta_1(0), \theta_2(0) = 0$. Friction coefficients are as follows:

$$k_{rx} = -1.2, \quad f_{rox} = 8, \quad \varepsilon_x = 0.01$$

Set the required dolly position as:

$$p_d=2\text{m}$$

To verify the advantages of the control effect of the proposed robust controller, the designed controller was observed together with the most widely used PD controller. The PD controller equation is:

$$F_x = F_{rx} - k_p\xi_x - k_d\dot{\xi}_x \tag{60}$$

positive control gains are k_p and $k_d \in \boldsymbol{R}^+$

The simulation is built according to Equation (60), which is shown in Figure 8.

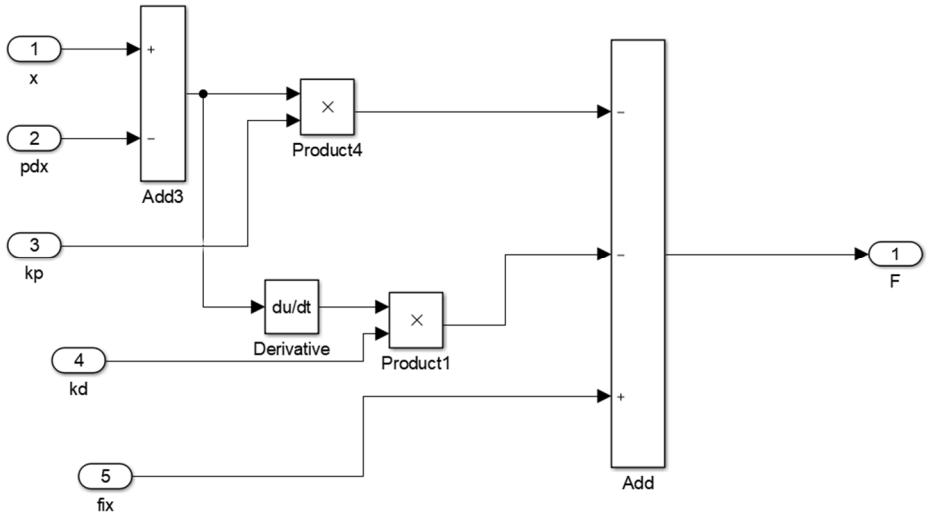

Figure 8. PD controller simulation module

The control gains of the proposed controller and the PD controller were compared in trials comparing the two systems were fully adjusted until the optimum performance of each was achieved the following seven control indicators were proposed:

(1) $\theta_{1_{max}}$ shows the hook's maximal swing during the transfer;

(2) $\theta_{2_{max}}$ shows the largest load swing amplitude possible during transmission;

(3) $\theta_{1_{res}}$ relates to the hook's full swing after the dolly has stopped;

(4) $\theta_{2_{res}}$ relates to the load's greatest swing after the dolly has stopped;

(5) p_d indicates the final position of the dolly;

(6) t_s denotes the moment when $\theta_1(t)$ and $\theta_2(t)$ come into the interval $|\theta_1|(t) \leq 0.5^{\circ}$ and $|\theta_2|(t) \leq 0.5^{\circ}$;

(7) $F_{x_{max}}$ indicates the maximum drive.

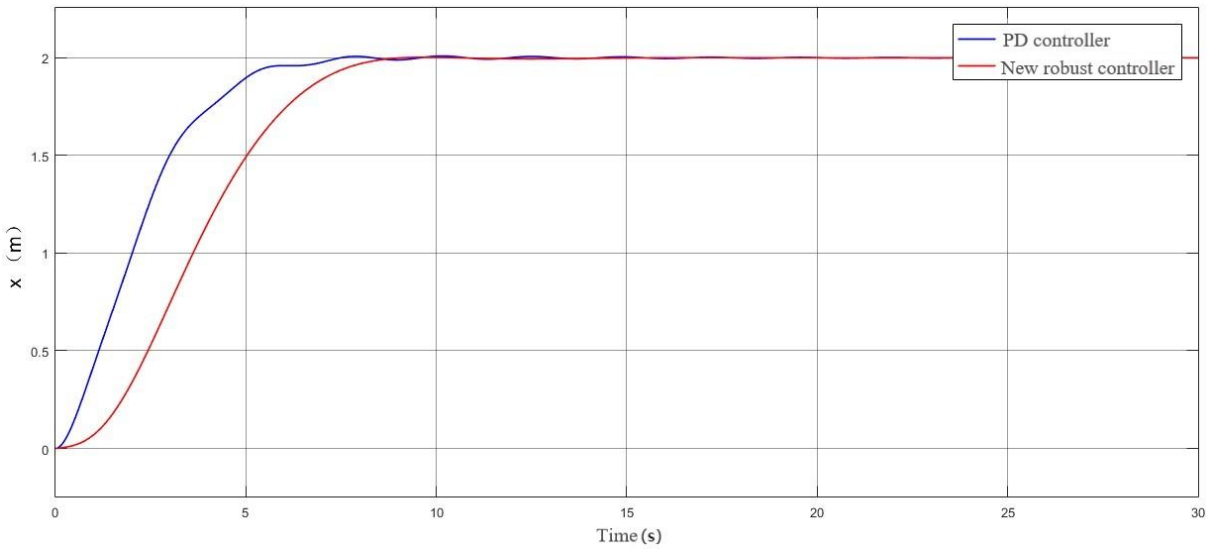

Figure 9. Comparison curve of two control methods in terms of dolly displacement X

Figure 9 displays the simulation results which indicates that the steady-state error of the PD control system is around 0.01 and there are constant oscillations, steeper waveforms in operation and large fluctuations in the data. The regulation time is 19.55s and the target position is reached at approximately 7.50s.

The robust controller design has a steady state error of 0 and the curve has good smooth characteristics during operation. The regulation time is 6.42s and the target position is reached at around 9.00s, which is a great improvement in speed and stability compared to the PD controller.

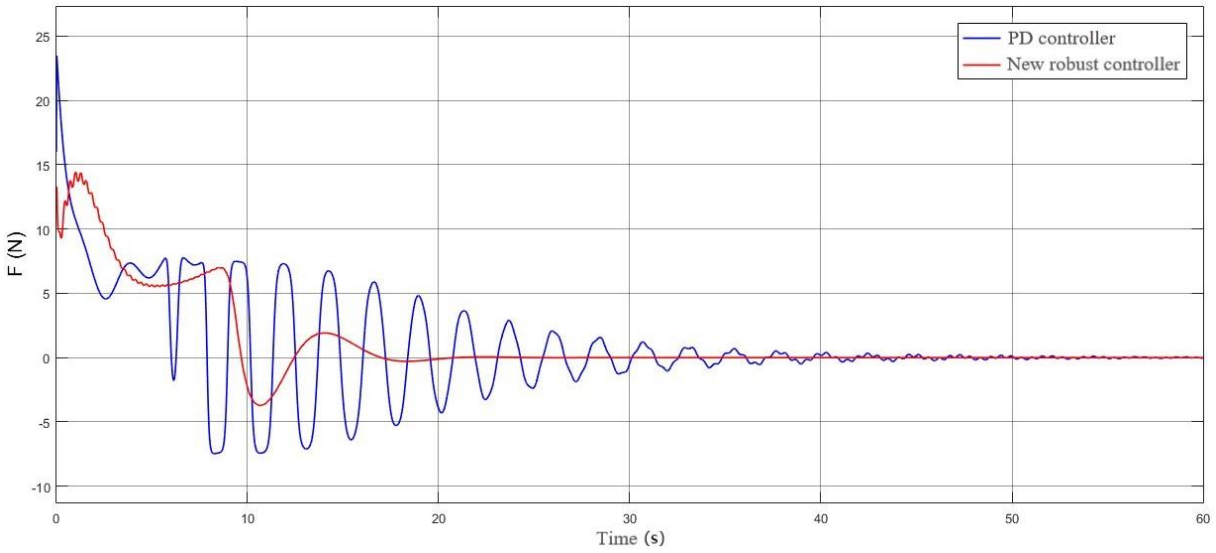

Figure 10. Comparison curves between the two control methods in terms of driving force F

Figure 10 displays the simulation results which indicates that the PD control method has an input maximum force of 23.45N and the horizontal driving force tends to 0 at about 43.53s, but there are still oscillations. In contrast, the designed robust controller gradually reaches 0 at about 20.55s and the maximum input drive force is 13.27N. In the comparison curve, it can be seen that the designed robust controller has a better control effect as the control force output is smaller and more stable than the PD controller and the convergence time of the force is shorter.

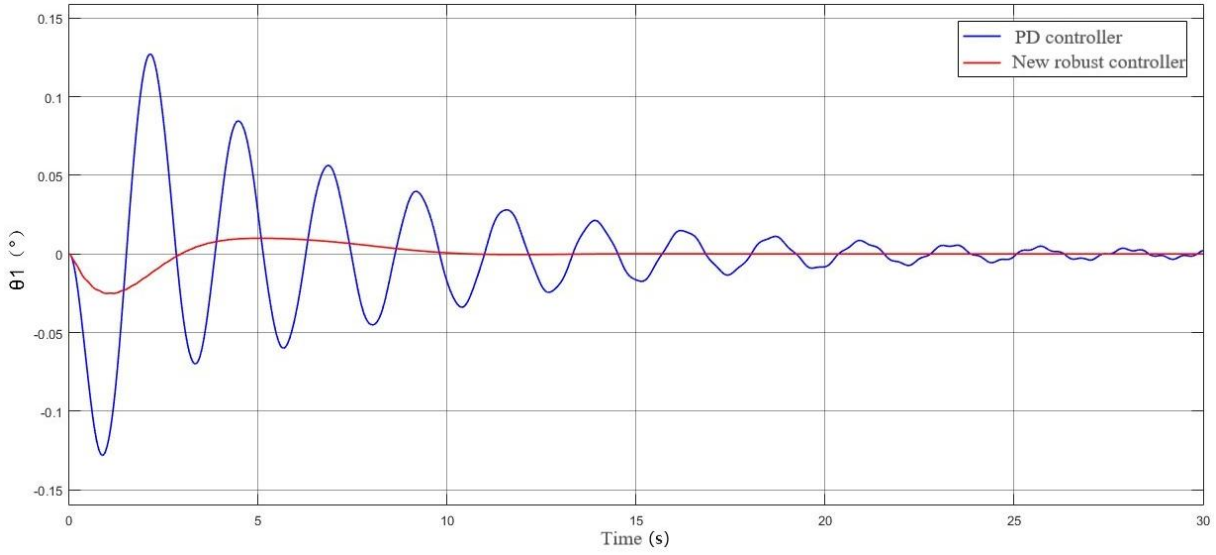

Figure 11. Comparison curve of the designed robust control method with the PD control method in terms of θ_1

As shown in Figure 11, the maximum pendulum angle obtained by simulation for the PD control method is approximately 7.34˚, with a more violent oscillation, returning to zero at approximately 28.55s, with a residual oscillation of approximately 0.2˚.

The designed robust control method has a maximum pendulum angle of approximately 1.44˚ and it took only one cycle to rapidly reduce the oscillation, which disappeared at approximately 10s and was the most stable.

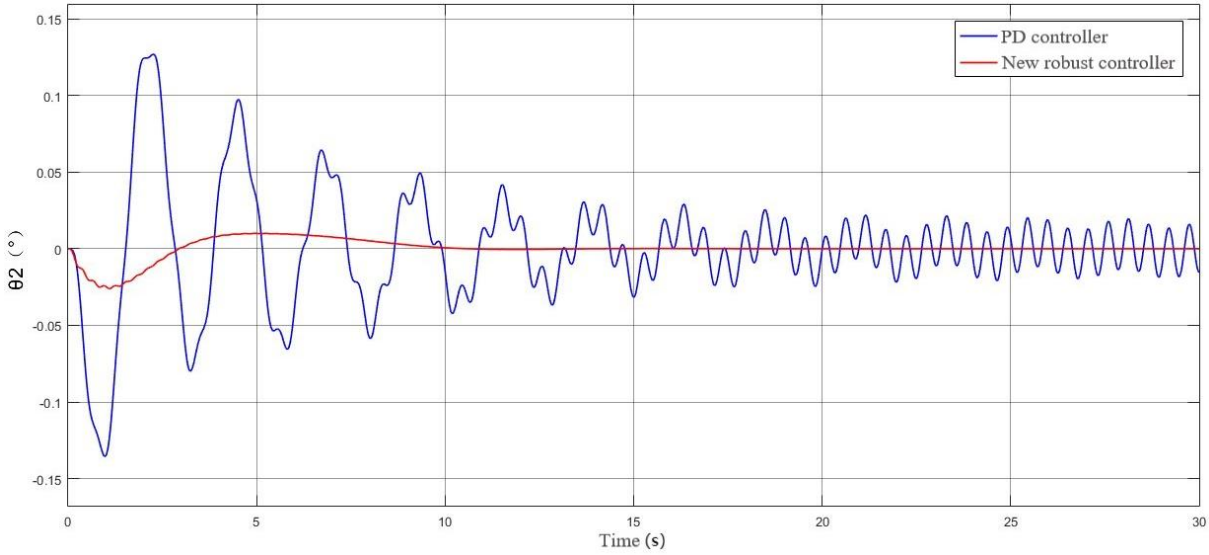

Figure 12. Comparison curve of the designed robust control method with the PD control method in terms of θ_2

As shown in Figure 12, the maximum pendulum angle obtained by simulation for the PD control method is about 7.75˚, the oscillation is more violent and the pendulum angle still does not return to zero within the 30s, with a residual oscillation of about 1.05˚.

The designed robust control method has a maximum swing angle of approximately 1.50˚ and again it only took one cycle to eliminate the swing, with the swing angle returning to zero at approximately 10.00s. It can be seen that the designed robust controller has a small swing of the load and hook during the control process and a strong swing elimination performance.

From this, we can see in Table 1 where the advantages of the robust controller lie.

Table 1. Control energy comparison

Controllers	New robust controller	PD controller
$\theta_{1_{\max}}(\circ)$	1.44	7.34
$\theta_{2_{\max}}(\circ)$	1.50	7.55
$\theta_{1_{\text{res}}}(\circ)$	0	0.2
$\theta_{2_{\text{res}}}(\circ)$	0	1.05
$p_d(m)$	2.00	2.00
$t_s(s)$	6.42	19.55
$F_{x_{\max}}(N)$	13.45	23.45

4.3 Robustness Testing

The primary goal of the simulation analysis in this work is to confirm that the suggested control approach is resistant to parameter fluctuations. As a result, there are four groups of numerical simulation tests:

(1) First, while keeping the control gains constant from the comparative tests of 4.3, we will test the control effectiveness of the developed control system by altering the load masses. The three load masses listed below are taken into account:

m_2=1KG, m_2=3KG, m_2=5KG

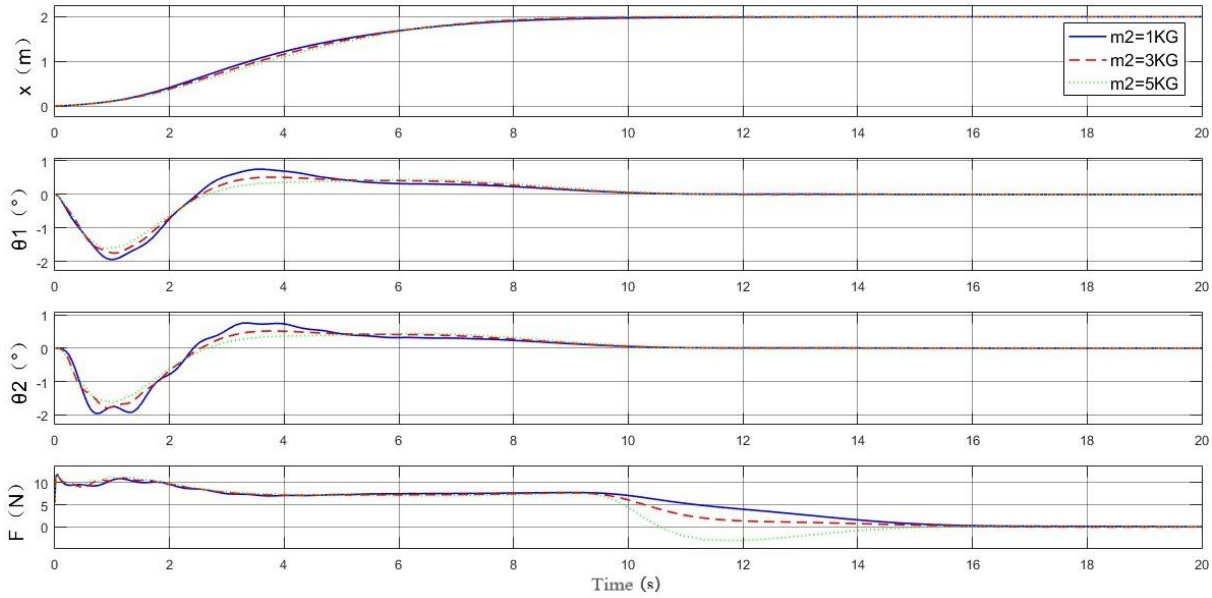

Figure 13. Simulation of new robust controllers on load quality

The results obtained are shown in Figure 13. For all three different load masses, the dolly can reach the target position accurately, consistently and quickly, and all can quickly suppress and eliminate secondary oscillations. The simulations have verified the superior robustness and stability of the method under various load masses.

(2) In this group, we will verify the control performance of the designed control system by varying the length of the sling. For this purpose, the following three sling lengths are used:

$$l_1$$=1m, l_1=2m, l_1=3m

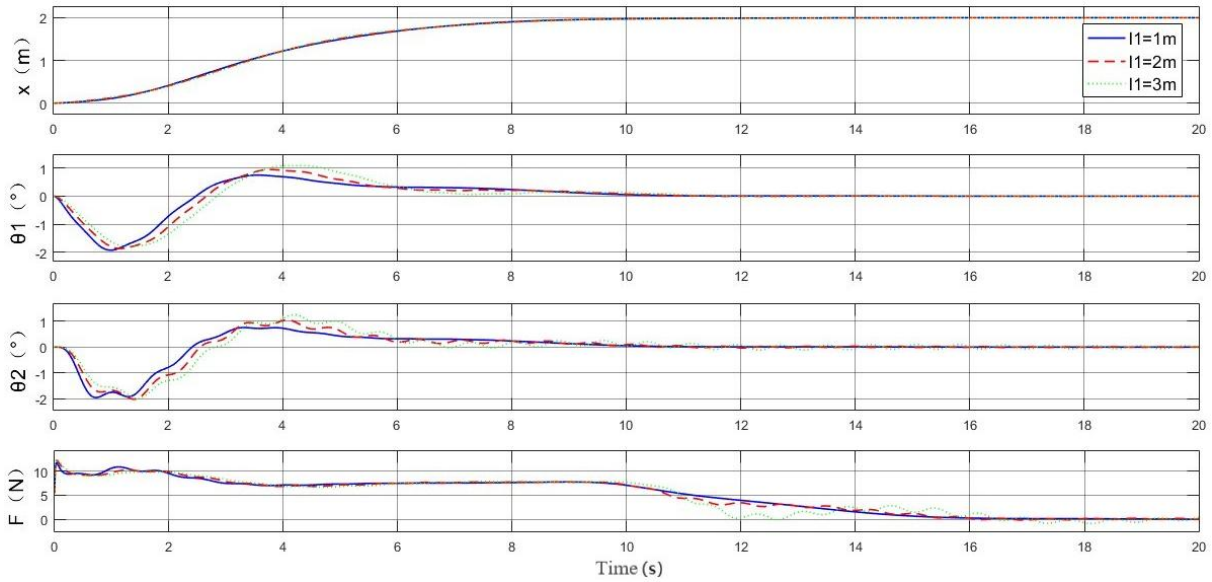

Figure 14. Simulation of the new robust controller on sling length

The results obtained are shown in Figure 14. The dolly positioning, load swing and hook swing cancellation are insignificantly affected by different sling lengths, which signifies that the designed controller is insensitive to the uncertainty in sling length.

(3) With the control gain remaining the same as in Table 1, we want to test the suggested controller's robustness at various desirable positions. The following 3 travel distances were established with this in mind:

$$p_d$$=1m, p_d=2m, p_d=3m

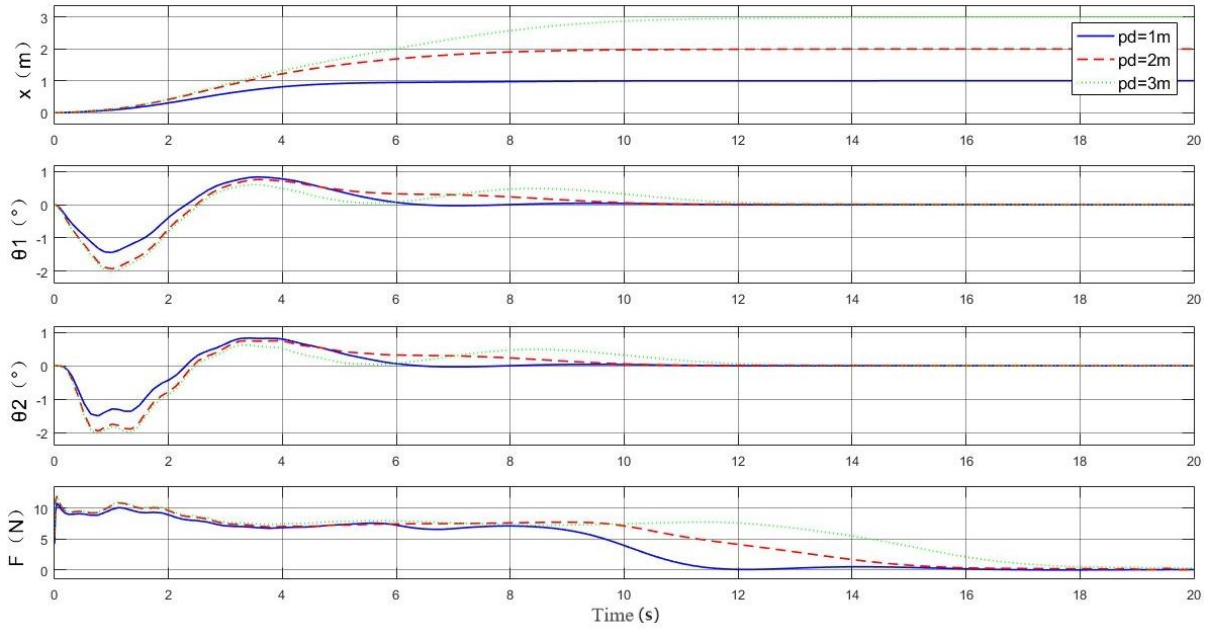

Figure 15. For the controller proposed in this paper, the results regarding the different desired target locations

As can be seen from Figure 15, the dolly can be driven precisely and quickly to the target position throughout the transport, although the target position changes and the load swing and hook swing are both less than 0.8°.

(4) The group added perturbations to the load swing to simulate external perturbations such as random perturbations throughout the transport. More precisely, we added impulsive perturbations between 9 ~ 10 s and sinusoidal perturbations between 15 ~ 16 s, all with an added perturbation amplitude of 2.

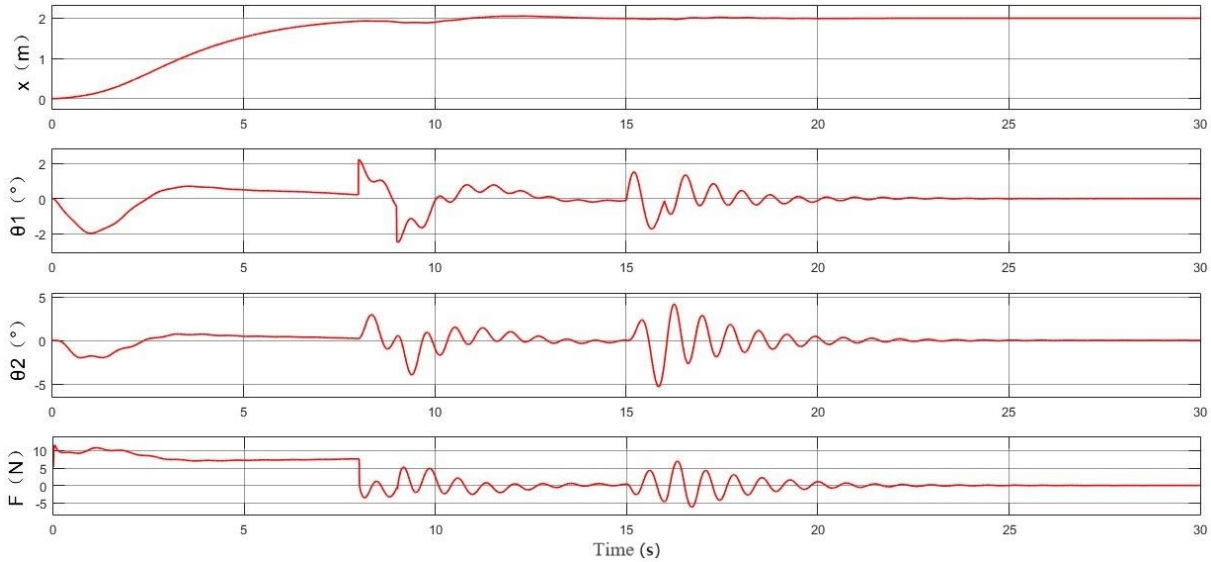

Figure 16. Results for the proposed controller under different perturbations

From Figure 16, it can be seen that the controller can achieve rapid suppression and cancellation of external disturbances, indicating that the proposed control method has strong robustness.

5. Conclusion

To solve the initial force problem of a double-pendulum overhead crane, a new energy-coupled control method is proposed that is simpler and more applicable than other controllers and is used to overcome the shortcomings of traditional control methods. In addition, a hyperbolic tangent function is introduced into the control law to ensure a smooth start of the dolly and to reduce the initial control force of the system. Through numerical simulations, it

is demonstrated that the designed controller exhibits good control effects with good robustness under various external disturbances and system parameters.

Moreover, the stability of this controller is investigated and verified in this paper by combining the Lyapunov method and Russell's invariance principle. Numerical simulations are carried out to compare the proposed controller with the PD controller and the results show that this new energy-coupled control method still has superior control performance and strong robustness with reduced initial control force for different load masses, sling lengths, target positions and external disturbances.

References

Al-Garni, A. Z., Moustafa, K. A., & Nizami, S. J., (1995). Optimal control of overhead cranes. *Control Engineering Practice, 3*(9), 1277-1284.

Butler, H., Honderd, G., & Van Amerongen, J., (1991). Model reference adaptive control of a gantry crane scale model. *IEEE Control Systems Magazine, 11*(1), 57-62.

Fang, Y., Ma, B., Wang, P., & Zhang, X., (2011). A motion planning-based adaptive control method for an underactuated crane system. *IEEE Transactions on control systems technology, 20*(1), 241-248.

Golovin, I., & Palis, S., (2019). Robust control for active damping of elastic gantry crane vibrations. *Mechanical Systems and Signal Processing*, 121, 264-278.

Guo, Q., Chai, L., & Liu, H., (2023). Anti-swing sliding mode control of three-dimensional double pendulum overhead cranes based on extended state observer. *Nonlinear Dynamics, 111*(1), 391-410.

He, W., Zhang, S., & Ge, S. S., (2013). Adaptive control of a flexible crane system with the boundary output constraint. *IEEE Transactions on Industrial Electronics, 61*(8), 4126-4133.

Hong, K. T., Huh, C. D., & Hong, K. S., (2003). Command shaping control for limiting the transient sway angle of crane systems. *International Journal of Control, Automation, and Systems, 1*(1), 43-53.

Karris, S. T., (2006). *Introduction to Simulink with engineering applications*. Orchard Publications.

Lee, H. H., (1998). *Modeling and control of a three-dimensional overhead crane*.

Lewis, D., Parker, G. G., Driessen, B., & Robinett, R. D., (1998, June). Command shaping control of an operator-in-the-loop boom crane. In *Proceedings of the 1998 American Control Conference*. ACC (IEEE Cat. No. 98CH36207) (Vol. 5, pp. 2643-2647). IEEE.

Li, P., Li, Z., & Yang, Y., (2012, December). The application research of ant colony optimization algorithm for intelligent control on special crane. In *2012 Second International Conference on Instrumentation, Measurement, Computer, Communication and Control* (pp. 999-1004). IEEE.

Li, X., Shao, X., & Chen, Z., (2021, May). The Research on Predictive Function Control of Double-Pendulum Overhead Crane. In *2021 33rd Chinese Control and Decision Conference* (CCDC) (pp. 5724-5731). IEEE.

Manson, G. A., (1982). Time-optimal control of an overhead crane model. *Optimal Control Applications and Methods, 3*(2), 115-120.

Miao, X., Zhao, B., Wang, L., & Ouyang, H., (2022). Trolley regulation and swing reduction of underactuated double-pendulum overhead cranes using fuzzy adaptive nonlinear control. *Nonlinear Dynamics, 109*(2), 837-847.

Ngo, Q. H., & Hong, K. S., (2010). Sliding-mode antisway control of an offshore container crane. *IEEE/ASME transactions on mechatronics, 17*(2), 201-209.

Neitzel, R. L., Seixas, N. S., & Ren, K. K., (2001). A review of crane safety in the construction industry. *Applied occupational and environmental hygiene, 16*(12), 1106-1117.

Ramli, L., Mohamed, Z., Abdullahi, A. M., Jaafar, H. I., & Lazim, I. M., (2017). Control strategies for crane systems: A comprehensive review. *Mechanical Systems and Signal Processing, 95*, 1-23.

Sakawa, Y., & Shindo, Y., (1982). Optimal control of container cranes. *Automatica, 18*(3), 257-266.

Sano, S., Ouyang, H., Yamashita, H., & Uchiyama, N., (2011). LMI approach to robust control of rotary cranes under load sway frequency variance. *Journal of System Design and Dynamics, 5*(7), 1402-1417.

Singhose, W. E., & Towell, S. T., (1998, September). Double-pendulum gantry crane dynamics and control. In *Proceedings of the 1998 IEEE International Conference on Control Applications* (Cat. No. 98CH36104) (Vol. 2, pp. 1205-1209). IEEE.

Smoczek, J., & Szpytko, J., (2008). A mechatronics approach in intelligent control systems of the overhead traveling cranes prototyping. *Information Technology and Control, 37*(2).

Solihin, M. I., Wahyudi, & Legowo, A., (2010). Fuzzy-tuned PID anti-swing control of automatic gantry crane. *Journal of Vibration and Control, 16*(1), 127-145.

Solihin, M. I., Kamal, M. A. S., & Legowo, A., (2008, May). Optimal PID controller tuning of automatic gantry crane using PSO algorithm. In *2008 5th International Symposium on Mechatronics and Its Applications* (pp. 1-5). IEEE.

Sun, N., Fang, Y., Zhang, Y., & Ma, B., (2011). A novel kinematic coupling-based trajectory planning method for overhead cranes. *IEEE/ASME Transactions on Mechatronics, 17*(1), 166-173.

Tam, V. W., & Fung, I. W., (2011). Tower crane safety in the construction industry: A Hong Kong study. *Safety science, 49*(2), 208-215.

Vaughan, J., Karajgikar, A., & Singhose, W., (2011, June). A study of crane operator performance comparing PD-control and input shaping. In *Proceedings of the 2011 American Control Conference* (pp. 545-550). IEEE.

Vaughan, J., Kim, D., & Singhose, W., (2010). Control of tower cranes with double-pendulum payload dynamics. *IEEE Transactions on Control Systems Technology, 18*(6), 1345-1358.

Wang, D., He, H., & Liu, D., (2017). Intelligent optimal control with critic learning for a nonlinear overhead crane system. *IEEE Transactions on Industrial Informatics, 14*(7), 2932-2940.

Wang, T., Tan, N., Qiu, J., Yu, Y., Zhang, X., Zhai, Y., ... & Scotti, F., (2021). Global-equivalent sliding mode control method for bridge crane. *IEEE Access, 9*, 160372-160382.

Wu, X., Xu, K., Lei, M., & He, X., (2020). Disturbance-compensation-based continuous sliding mode control for overhead cranes with disturbances. *IEEE Transactions on Automation Science and Engineering, 17*(4), 2182-2189.

Xiao, F., Honma, Y., & Kono, T., (2005). A simple algebraic interface capturing scheme using hyperbolic tangent function. *International journal for numerical methods in fluids, 48*(9), 1023-1040.

Yavuz, H., & Beller, S., (2021). An intelligent serial connected hybrid control method for gantry cranes. *Mechanical Systems and Signal Processing, 146*, 107011.

Zhang, M., Zhang, Y., & Cheng, X., (2019). An enhanced coupling PD with sliding mode control method for underactuated double-pendulum overhead crane systems. *International Journal of Control, Automation and Systems, 17*(6), 1579-1588.

Zhang, M., Zhang, Y., & Cheng, X., (2019). An enhanced coupling PD with sliding mode control method for underactuated double-pendulum overhead crane systems. *International Journal of Control, Automation and Systems, 17*(6), 1579-1588.

Zhang, X., Fang, Y., & Sun, N., (2014). Minimum-time trajectory planning for underactuated overhead crane systems with state and control constraints. *IEEE Transactions on Industrial Electronics, 61*(12), 6915-6925.